Microcirculation
The Official Journal of the Microcirculatory Society, Inc., the British Microcirculation Society, and the Australia & New Zealand Microcirculation Society

DOI:10.1111/micc.12141

Original Article

Non-Newtonian Flow of Blood in Arterioles: Consequences for Wall Shear Stress Measurements

KRISHNA SRIRAM,* MARCOS INTAGLIETTA,† AND DANIEL M. TARTAKOVSKY*

*Department of Mechanical and Aerospace Engineering, University of California, San Diego, California, USA; †Department of Bioengineering, University of California, San Diego, California, USA

Address for correspondence: Daniel M. Tartakovsky, Department of Mechanical and Aerospace Engineering, University of California, San Diego, 9500 Gilman Drive, La Jolla, CA 92093, USA. *E-mail:* dmt@ucsd.edu

Received 25 February 2014; accepted 2 April 2014.

ABSTRACT

Objective: Our primary goal is to investigate the effects of non-Newtonian blood properties on wall shear stress in microvessels. The secondary goal is to derive a correction factor for the Poiseuille-law-based indirect measurements of wall shear stress.

Methods: The flow is assumed to exhibit two distinct, immiscible and homogeneous fluid layers: an inner region densely packed with RBCs, and an outer cell-free layer whose thickness depends on discharge hematocrit. The cell-free layer is assumed to be Newtonian, while rheology of the RBC-rich core is modeled using the Quemada constitutive law.

Results: Our model provides a realistic description of experimentally observed blood velocity profiles, tube hematocrit, core hematocrit, and apparent viscosity over a wide range of vessel radii and discharge hematocrits.

Conclusions: Our analysis reveals the importance of incorporating this complex blood rheology into estimates of WSS in microvessels. The latter is accomplished by specifying a correction factor, which accounts for the deviation of blood flow from the Poiseuille law.

Key words: blood rheology, hematocrit, shear thinning, plasma layer, apparent viscosity, shear stress

Abbreviations used: CFL, cell-free layer; MRI, magnetic resonance imaging; NO, nitric oxide; PIV, particle image velocimetry; RBC, red blood cell; RMSE, root mean square error; WSS, wall shear stress.

Please cite this paper as: Sriram K, Intaglietta M, Tartakovsky DM. Non-Newtonian flow of blood in arterioles: Consequences for wall shear stress measurements. *Microcirculation* **21**: 628–639, 2014.

INTRODUCTION

Velocity profiles of blood flowing in glass tubes [1,10,18] and *in vivo* [3,15,36] are observed to be blunted, rather than parabolic. Both the CFL [14,18] and non-Newtonian behavior of blood [19,22,26,34] in the microcirculation have been used to explain the experimentally observed bluntness of blood velocity profiles in narrow glass tubes [1,10,18] and *in vivo* microvessels [3,15,18,36].

Blunting of the velocity profiles observed in microvessels affects the overall rate of energy dissipation by the flow and the distribution of shear rates across the vessel cross section. Of particular physiological significance is the shear stress developed at the microvessel wall. It modulates the production of shear-stress-dependent materials by the endothelium, a significant effect due to the large endothelial surface of the microcirculation [2,16,23]. The bluntness of blood velocity profiles has significant implications on indirect measurements of WSS, which are typically inferred from direct measurements of centerline velocity and vessel radius by invoking the Poiseuille law [5,13,28]. The mismatch between the experimentally observed blunt velocity profiles and their parabolic counterparts predicted by the Poiseuille law introduces interpretive errors in WSS measurement [13,28].

A typical CFL thickness is on the order of 1 μm [14,24,27,35]. It is relatively insensitive to vessel radius, but decreases significantly with hematocrit [9,29,35]. While plasma in the CFL can be treated as a Newtonian fluid, the RBC-rich core displays non-Newtonian shear-thinning properties. In this study, we assume a general functional dependence of the CFL thickness on hematocrit and then calculate velocity profiles of blood flow through a tube, comprising two discrete fluid layers: the non-Newtonian RBC core and the CFL (which is assumed to be Newtonian).

Experimental work on blood rheology has demonstrated the dependence of blood viscosity on shear rate and hematocrit, showing that the relationship between shear stress and shear rate for blood is non-linear (and non-Newtonian), with the shear-thinning properties [7,19,22]

that are enhanced by increasing hematocrit. This shear-thinning rheology of blood in the RBC core is represented in our flow model via the Quemada rheological model. The Quemada model is a three-parameter constitutive rheological model that accurately describes shear-thinning blood rheology over a wide range of shear rates and hematocrit [19,22,26]. Due to this robustness, the Quemada model is superior to other blood rheological models of comparable complexity [19] and was hence utilized in our flow model.

Previous mathematical models of blood flow in microvessels have typically treated both fluid layers (the CFL and RBC core) as Newtonian fluids, with the viscosity of the RBC core being larger than the viscosity of the CFL [21,31,33]. Our model builds on these previous studies; we compare results of our non-Newtonian model with those of the two-layer Newtonian model and demonstrate that significant differences between the two models exist. We demonstrate that our model is a significant improvement over previous Newtonian models, more accurately predicting CFL thickness, velocity profiles, and apparent viscosities.

We then leverage our flow model to develop a general method for correcting the experimental estimation of WSS. Typically, WSS in a blood vessel is estimated in experimental studies by measuring the centerline velocity and the vessel radius; with these values, the WSS is then calculated using the Poiseuille law [5,13,28]. The problem with this approach is that blood flow in microvessels does not follow the Poiseuille law (due to the inhomogeneous and non-Newtonian behaviors discussed above). This introduces errors in the measurement of WSS [13,28].

These errors may be avoided by direct measurement of velocity profiles, using methods such as in [18]. This allows precise estimation of shear rate at the vessel wall; for a known plasma viscosity, WSS can then be calculated once wall shear rate is known. The difficulty with this alternative is that direct measurement of velocity profiles is a complicated task; repeatedly measuring velocity profiles every time WSS estimates are needed is relatively impractical (and expensive) with current technology and experimental techniques [13].

In this study, we compute the magnitude of these WSS estimation errors arising from the use of the Poiseuille law and demonstrate that these errors are significant. We propose two methods to eliminate these errors: An iterative numerical algorithm which leverages our flow model, and the use of a simple correction factor that can be incorporated into the Poiseuille law. Given a rheological model of the RBC-rich core, both approaches allow one to infer WSS from measurements of vessel radius, centerline velocity, and discharge hematocrit.

MATHEMATICAL MODEL OF BLOOD FLOW IN ARTERIOLES

Symbols used	
R, r	Vessel radius and radial coordinate
μ_p	Plasma viscosity
γ_c, k_0, and k_∞	Parameters in the Quemada rheological model
μ, μ_{eff}, μ_{rel}	Medium, effective medium, and relative medium viscosity
τ, τ_w	Shear stress and WSS
δ	CFL thickness
Q	Flow rate of blood in blood vessel
γ	Shear rate
H, H_c, H_d, H_t	Localized, core, discharge, and tube hematocrit
J	Pressure gradient
v_z	Axial velocity
v_{max}	Centerline (maximum) velocity
ϕ	WSS correction factor

We consider steady-state blood flow in an arteriole of fixed radius R. The flow is driven by an externally imposed pressure gradient J, with no-slip boundary conditions prescribed at the (nondeformable) vessel walls. Blood is treated as a two-layer inhomogeneous fluid: An RBC-rich core region near the vessel centerline [31,33] occupies the cylinder of radius $(R - \delta)$ and a CFL of thickness δ occupies the rest of the vessel (Figure 1). Plasma in the CFL is modeled as a Newtonian fluid with constant viscosity μ_p, independent of both hematocrit and shear rate γ. Hematocrit distribution in the RBC-rich core is assumed to be uniform. The Quemada rheological model [19,22,26] is used to describe the non-Newtonian, shear-thinning behavior of the RBC-rich core.

The Quemada constitutive law postulates a nonlinear relationship between shear stress τ and shear rate γ in the RBC-rich core,

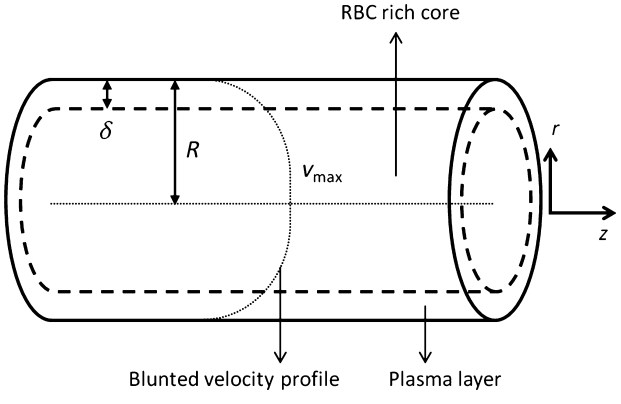

Figure 1. CFL and RBC-rich core in an arteriole. The CFL is occupied by plasma, a Newtonian fluid whose viscosity is lower than that of the non-Newtonian fluid comprising the RBC-rich core.

$$\tau = \frac{\gamma \mu_p}{(1 - kH_c/2)^2}, \quad k = \frac{k_0 + k_\infty \sqrt{\gamma/\gamma_c}}{1 + \sqrt{\gamma/\gamma_c}}. \tag{1}$$

The model parameters γ_c, k_0, and k_∞ vary with core hematocrit H_c (the value of hematocrit H in the RBC-rich core) [7,22]. We fit the parameter data reported in [22] with second-degree polynomials in H_c. Figure 2 exhibits both the data and the fitted curves (with the goodness of the fit R^2 exceeding 0.99 for all three curves). The Quemada model (Eq. 1) reduces to a linear (Newtonian) relationship between τ and γ when either H_c is small or γ is large.

The normalized (dimensionless) effective viscosity μ_{eff} of blood is defined from Eq. (1) as

$$\mu_{eff} = \frac{\tau}{\gamma \mu_p} = \frac{1}{(1 - kH_c/2)^2}. \tag{2}$$

According to this expression, the normalized effective viscosity μ_{eff} of blood in the core region decreases with increases in shear rate γ and increases with increases in core hematocrit H_c (Figure 3). At large values of γ (above 200 per second), the viscosity is approximately constant and the fluid is essentially Newtonian. Regardless of the fluid properties, the Cauchy equations of motion for steady (or pseudo-steady for low Womersley numbers), axisymmetric laminar flow have the form

$$0 = -J + \frac{1}{r}\frac{\partial}{\partial r}(r\tau). \tag{3}$$

Integrating this equation across the RBC-rich core (from 0 to $R - \delta$) and across the CFL (from $R - \delta$ to R) yields, respectively,

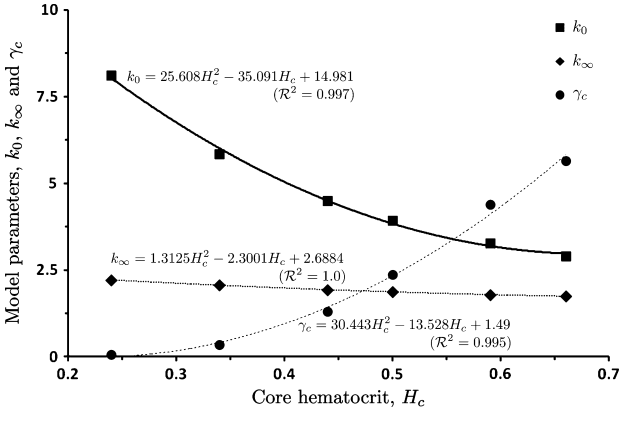

Figure 2. The data reported in [22] show the dependence of the Quemada model parameters γ_c, k_0, and k_∞ on hematocrit in the RBC core, H_c. These data are fitted with second-degree polynomials in H_c.

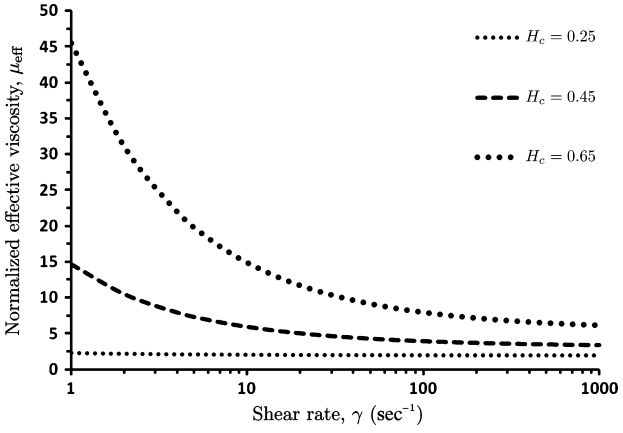

Figure 3. Variation in normalized (dimensionless) effective viscosity μ_{eff} of blood in the core region, with shear rate γ and core hematocrit H_c.

$$\tau(r) = \frac{Jr}{2} + \frac{C_1}{r}, \quad 0 \le r \le R - \delta \tag{4}$$

and

$$\tau(r) = \frac{Jr}{2} + \frac{C_2}{r}, \quad R - \delta \le r \le R, \tag{5}$$

where C_1 and C_2 are constants of integration. As the shear stress $\tau(r)$ must remain finite throughout the blood vessel, including its centerline $r = 0$, we set $C_1 = 0$. The continuity of the shear stress at the interface between the two fluids (at $r = R - \delta$) requires $C_2 = 0$. Therefore, the shear stress $\tau(r)$ is given by

$$\tau(r) = \frac{Jr}{2}, \quad 0 \le r \le R \tag{6}$$

throughout the blood vessel.

Combining Eqs. (6) and (1) yields an implicit expression for the radial distribution of shear rate $\gamma(r)$ within the RBC-rich core,

$$\gamma = \frac{Jr}{2\mu_p}\left(1 - \frac{H_c}{2}\frac{k_0 + k_\infty\sqrt{\gamma/\gamma_c}}{1 + \sqrt{\gamma/\gamma_c}}\right)^2, \quad 0 \le r \le R - \delta. \tag{7}$$

As the CFL is occupied by plasma (a Newtonian fluid with viscosity μ_p), $\tau = \mu_p\gamma$ for $R - \delta \le r \le R$ and Eq. (6) yields

$$\gamma = \frac{Jr}{2\mu_p}, \quad R - \delta \le r \le R. \tag{8}$$

Equations (7) and (8) are coupled by the continuity of flow velocity at the interface $r = R - \delta$ separating the RBC-rich core and the CFL,

$$v_z^+ = v_z^-, \tag{9}$$

where v_z is the flow velocity, and the superscripts + and − indicate the core and plasma velocities on either side of the interface, respectively. The flow velocity is related to the corresponding shear rate by $\gamma = dv_z/dr$. At the vessel wall ($r = R$), we impose a no-slip boundary condition, $v_z(R) = 0$.

Given a value of the CFL thickness δ, both the shear rate $\gamma(r)$ and the flow velocity $v_z(r)$ are calculated by solving Eqs. (7–9). The data reported in [9,29] suggest that δ is relatively insensitive to the blood vessels radius R, but decreases appreciably with the discharge hematocrit H_d. The latter is related to the core hematocrit H_c by mass conservation [33],

$$H_c \int_0^{R-\delta} v_z(r) r dr = H_d \int_0^R v_z(r) r dr. \tag{10}$$

While one can choose any functional relation between δ and H_d, for the sake of concreteness we adopt a polynomial relationship

$$\delta = a_2 H_d^2 + a_1 H_d + a_0. \tag{11}$$

The parameters a_0, a_1, and a_2 are determined by fitting our model predictions to the measurements of apparent viscosity [25]. An initial guess for δ ($a_2 = 0$, $a_1 = 0$, and $a_0 = 1$ μm, which gives $\delta = 1$ μm) is refined by using the procedure outlined in section "Model Calibration."

NUMERICAL ALGORITHM FOR CALCULATING VELOCITY PROFILES

For given values of the discharge hematocrit H_d and the pressure gradient J, we use the following algorithm to compute the shear rate $\gamma(r)$ and the flow velocity $v_z(r)$:

1. Make an initial guess for H_c. (In the simulation reported below, the linear relationship $H_c = 0.9797 H_d + 0.0404$ [33] is used as an initial guess.)
2. Calculate the value of δ by using Eq. (11).
3. Compute the shear rate $\gamma(r)$ in the RBC-rich core and the CFL by using Eqs. (7) and (8), respectively.
4. Compute the flow velocity $v_z(r) = \int_0^r \gamma(r')dr'$.
5. Refine the previous guess for H_c by using Eq. (10).
6. Repeat steps 3–5 until the absolute difference between the values of H_c obtained from two sequential iterations is smaller than prescribed tolerance Δ (in the simulations reported below we set $\Delta = 10^{-6}$).

MODEL CALIBRATION

Pries, Neuhaus, and Gaehtgens [25] compiled a number of measurements of human blood viscosity conducted in tubes of various radii R for several values of discharge hematocrit H_d. We use these data to calibrate our model, i.e., to determine the values of parameters a_0, a_1, and a_2 in Eq. (11). That is accomplished in three steps as follows.

The first step is to evaluate the relative (dimensionless) apparent viscosity μ_{rel} that is defined as [25]

$$\mu_{rel} = \frac{\pi J R^4}{8 Q \mu_p}. \tag{12}$$

This quantity is routinely inferred from experiments by measuring Q and invoking the Poiseuille law. Instead, for a given value of the CFL thickness δ, we compute Q from the flow velocity v_z determined in section "Algorithm for Inference of WSS from Blood Flow Measurements" as

$$Q = 2\pi \int_0^R v_z(r) r dr. \tag{13}$$

This calculation of Q is then used in Eq. (12) to obtain the value of μ_{rel} associated with an assumed value of δ. Figure 4 exhibits the resulting dimensionless apparent viscosity μ_{rel} as a function of vessel radius R for discharge hematocrit $H_d = 0.45$ and several values of the CFL thickness δ.

The second step is to compare the relative apparent viscosity curves $\mu_{rel} = \mu_{rel}(R)$ in Figure 4 with their counterparts predicted by the data-fitted curve of Pries, Neuhaus, and Gaehtgens [25], $\mu_{Pr} = \mu_{Pr}(R)$. The latter is given by

$$\mu_{Pr} = 1 + (\mu_{Pr,0.45} - 1)\frac{(1 - H_d)^\alpha - 1}{(1 - H_d)^\alpha - 1}, \tag{14a}$$

where $\mu_{Pr,0.45}$ is the dimensionless apparent viscosity at reference discharge hematocrit $H_d = 0.45$ fitted with a curve

$$\mu_{Pr,0.45} = 220 e^{-1.3(2R)} + 3.2 - 2.44 e^{-0.06(2R)^{0.064}} \tag{14b}$$

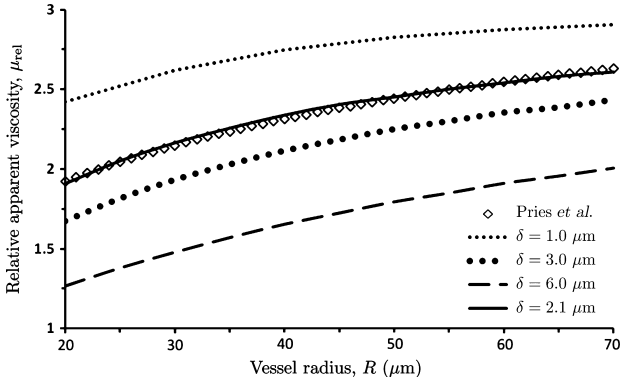

Figure 4. Dependence of relative apparent viscosity μ_{rel} on vessel radius R, for discharge hematocrit $H_d = 0.45$ and several values of the CFL thickness δ. Also shown is the dimensionless apparent viscosity obtained with the data-fitted curve (Eq. 14) of Pries, Neuhaus, and Gaehtgens [25].

and

$$\alpha = (0.8 + e^{-0.075(2R)})\left[-1 + \frac{1}{1 + 10^{-11}(2R)^{12}}\right] + \frac{1}{1 + 10^{-11}(2R)^{12}}. \quad (14c)$$

In the relations above, R is reported in μm and α is dimensionless. The value of the CFL thickness δ that provides the best agreement between the two approaches is selected. For discharge hematocrit $H_d = 0.45$ used in Figure 4, this value is $\delta = 2.1$ μm. The fact that agreement between our model (Steps 1 and 2) and the Pries, Neuhaus, and Gaehtgens [25] curves persists over a wide range of vessel radii R serves to validate our assumption that the CFL thickness δ is a function of discharge hematocrit H_d alone.

The final step consists of repeating the above procedure for multiple values of discharge hematocrit H_d, tabulating the δ vs. H_d values, and fitting the second-degree polynomial (Eq. 11) to the resulting dataset. This step results in

$$\delta = -2.265H_d^2 - 1.4377H_d + 3.2131, \quad (15)$$

where values of δ are in μm. The use of the parameterized constitutive law (Eq. 15) in our model yields predictions of apparent viscosity $\mu_{rel}(R)$ that are in close agreement with their counterparts based on the Pries, Neuhaus, and Gaehtgens [25] calculations over a physiologically relevant range of discharge hematocrit H_d and microvessel radii R (Figure 5).

MODEL VALIDATION

To validate our model, we compare its predictions of the CFL width, blood velocity profiles, and tube hematocrit (defined below) with their experimentally observed counterparts. These comparisons are carried out on previously published experimental data that were not used to parameterize our model.

CFL Thickness

The values of CFL thickness δ predicted with the constitutive law (Eq. 15) fall within a generally accepted range of around 2–3 μm [14,24,27,35]. Figure 6 provides a further confirmation of the ability of our model to predict the CFL thickness for a wide range of microvessel radii. It compares the dependence of the relative CFL thickness δ/R on vessel radius R predicted with our model and observed in the experiments [24,27,35], for discharge hematocrit $H_d = 0.45$. Our model qualitatively captures the observed decrease in the relative CFL thickness δ/R with vessel radius R, underestimating the observed CFL thickness by 13% for $R = 15$ μm, 20% for $R = 30$ μm, and 25% for $R = 47$ μm. This level of agreement is significantly better than that achieved with the earlier models [9,31,33].

Flow Velocity Profiles

We compare the velocity profile $v_z(r)$ predicted with our model with its counterpart constructed from experimental micro-PIV measurements of velocity profiles of human blood flow in glass tubes [18]. Figure 7 shows the predicted and observed velocity profiles for discharge hematocrit $H_d = 0.335$, pressure gradient $J = 3732$ dyn/cm^3, and tube radius $R = 27.1$ μm used in the experiment [18]. The mean square root error between the data and predictions is 0.068.

A location of the kink in the experimentally measured velocity profile ($r/R \approx 0.92$ in Figure 7) indicates a position of the core/CFL interface ($r = R - \delta$). Applied to the experimental data in [18] (see Figure 7), this yields $\delta \approx 2.2$ μm. This estimate of the CFL thickness δ is much

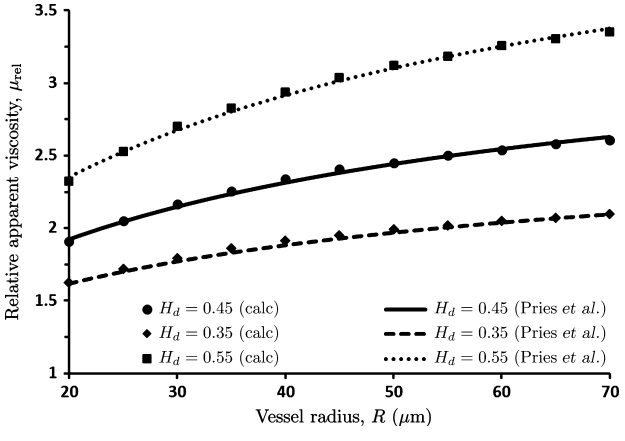

Figure 5. Relative apparent viscosity μ_{rel} calculated with our model and the data-fitted curve of Pries, Neuhaus, and Gaehtgens [25] over physiologically relevant ranges of microvessel radii R and discharge hematocrit H_d.

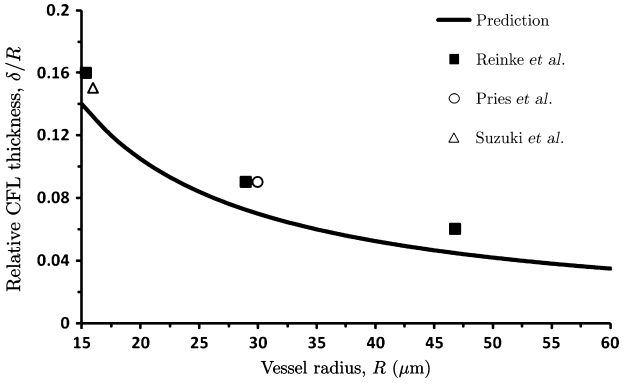

Figure 6. Predicted and experimentally observed values of relative CFL thickness δ/R as a function of vessel radius R for discharge hematocrit $H_d = 0.45$. Experimental data are from [24,27,35].

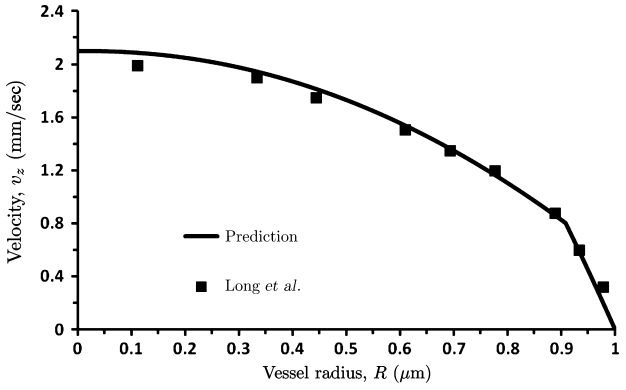

Figure 7. Predicted and observed velocity profiles, plotted against normalized radial distance from centerline $r = R$, for discharge hematocrit $H_d = 0.335$, pressure gradient $J = 3732$ dyn/cm^3, and tube radius $R = 27.1$ μm used in [18].

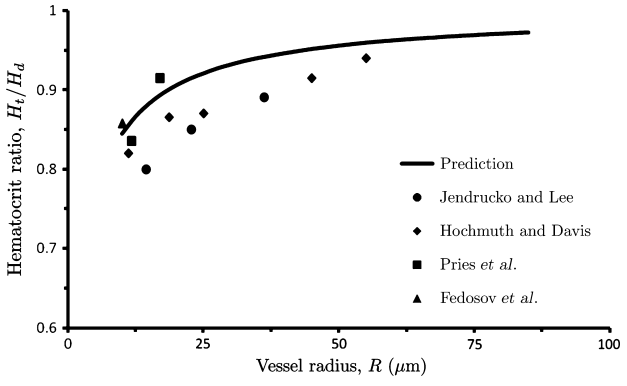

Figure 8. Calculated and measured values of H_t/H_d as a function of vessel radius R, for $H_d = 0.405$. Data are from [9,11,12,24].

closer to that predicted by our model ($\delta = 2.48$ μm) than values for δ reported in earlier models [9,31].

Tube Hematocrit

As a final validation test, we investigate the ability of our model to reproduce measurements of tube hematocrit H_t, which is defined as the average (over a vessel's cross section) hematocrit [31],

$$H_t \equiv \frac{2}{R^2}\int_0^R H(r) r dr. \tag{16}$$

In the two-layer fluid model under consideration, $H(r) = H_c$ inside the RBC-rich core ($0 \le r \le R - \delta$) and $H(r) = 0$ inside the CFL ($R - \delta < r \le R$). Therefore, this equation predicts a linear relationship between tube hematocrit H_t and core hematocrit H_c [31],

$$H_t \equiv \frac{(R-\delta)^2}{R^2} H_c. \tag{17}$$

Measurements of tube hematocrit H_t are typically reported relative to discharge hematocrit H_d, i.e., as the ratio H_t/H_d. This ratio is observed to be smaller than unity, a phenomenon that is referred to as the Fahraeus effect [8]. The disparity between values of tube hematocrit H_t and discharge hematocrit H_d is due to the presence of the CFL; the difference between the three types of hematocrit diminishes, $H_t \approx H_c \approx H_d$, as $\delta/R \to 0$.

Figure 8 shows the observed [9,11,12,24] and computed dependence of H_t/H_d on vessel radius R for $H_d = 0.405$. While the mean RMSE between the data and predictions is relatively large (RMSE = 0.052), our model captures the key features of this dependence. The ratio H_t/H_d increases with vessel radius R, approaching its limiting value of 1 at large R ($\delta/R \to 0$). Moreover, the absolute difference between our calculations and the experimental data does not exceed 11% and is significantly smaller (less than 4%) for many data points over a wide range of vessel diameters.

SIMULATION RESULTS

The results presented in this section are for pressure gradient $J = 40{,}000$ dyn/cm^3. The latter corresponds to WSS of 40 dyn/cm^2 at $R = 20$ μm, a value consistent with *in vivo* WSS measurements [17] typically observed in the microcirculation.

Flow Velocity Profiles

The velocity profiles $v_z(r)$ computed with our model are blunted, rather than parabolic (Figure 9). Each profile is normalized with the corresponding maximum (centerline) velocity v_{max}. In a blood vessel of radius $R = 20$ μm, $v_{max} = 14.9$, 11.0 and 7.4 mm/sec for discharge hematocrit $H_d = 0.35$, 0.45 and 0.55, respectively. In a blood vessel of radius $R = 40$ μm, these increase to $v_{max} = 25.1$, 39.0, and 55.0 mm/sec for the respective values of discharge hematocrit H_d. Figure 9 also shows the parabolic velocity profiles that arise from the Poiseuille solution for pipe flow.

The bluntness of the velocity profiles increases with the discharge hematocrit H_d due to two reasons. First, the non-Newtonian behavior of blood becomes more pronounced as hematocrit increases. Second, higher levels of hematocrit lead to higher viscosities of the RBC-rich core, increasing the contrast between the viscosities of the core and the CFL.

Figure 9 also reveals that the non-Newtonian behavior of blood is less pronounced, i.e., the deviation from the Poiseuille's parabolic velocity profile is less significant, in larger vessels. This observation is in line with the standard modeling practice of modeling blood in large vessels as a Newtonian fluid.

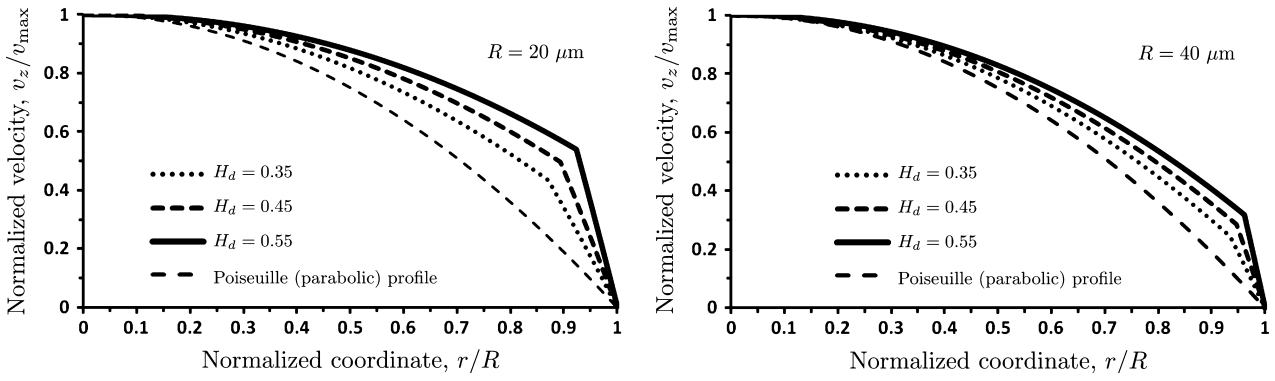

Figure 9. Velocity profiles $v_z(r/R)$, normalized with corresponding maximum (centerline) velocities v_{max}, for vessel radii R = 20 μm (left) and 40 μm (right) and several values of discharge hematocrit H_d. Also shown is the (normalized) parabolic velocity profile predicted by the Poiseuille law.

Relationship Between Core and Discharge Hematocrits

Mass conservation of RBCs, as expressed by Eq. (24), establishes a linear relationship between the core (H_c) and discharge (H_d) hematocrits (see also, [33]). In addition, it defines the (nonlinear) dependence of the hematocrit ratio H_c/H_d on the blood vessel radius R. This dependence, computed with the algorithm of section "Algorithm for Inference of WSS from Blood Flow Measurements", is displayed in Figure 10 for several values of the discharge hematocrit H_d. As vessel radii become larger, the difference between the core and discharge hematocrits becomes less significant, i.e., the ratio $H_c/H_d \to 1$.

Comparison with the Two-Layer Newtonian Model

Several previous studies, e.g., [21, 31, 33], treated blood as a two-phase fluid (as we do), but assumed that both the RBC-rich core and the CFL exhibit Newtonian behavior. Comparison of these models with ours sheds light on the impact of the non-Newtonian effects on predictions of both the flow velocity v_z and the relative apparent viscosity μ_{rel}.

Figure 11 shows the velocity profiles $v_z(r)$ in a vessel of radius R = 20 μm, computed with the two-phase Newtonian model [21,31,33] (see Appendix) and our two-layer Quemada model. Each of these velocity profiles is normalized with its maximum (centerline) velocity v_{max} (=1.845 and 1.286 mm/sec for the Newtonian and Quemada and models, respectively). Both profiles differ significantly from the parabolic profile predicted by the Poiseuille law. The Newtonian assumption significantly overestimates flow velocity (v_{max} by about 50%) and underestimates the degree of bluntness of the velocity profile. This is despite the fact that the CFL thickness δ predicted with our model is smaller than that suggested in [31]. It is worthwhile emphasizing that the values of δ predicted with our model fall within the experimentally observed range (1.5–3.0 μm), whereas the estimates of δ in [31] (3.5–4.0 μm) do not.

Figure 12 exhibits the dependence of relative apparent viscosity μ_{rel} on vessel radius R predicted with the two-phase

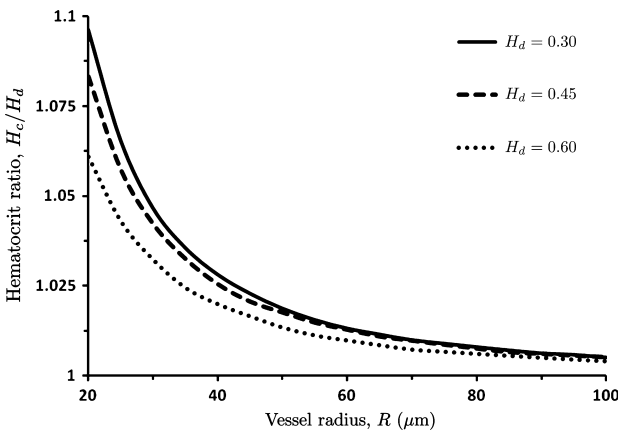

Figure 10. Hematocrit ratio H_c/H_d as a function of blood vessel radius R for several values of discharge hematocrit H_d.

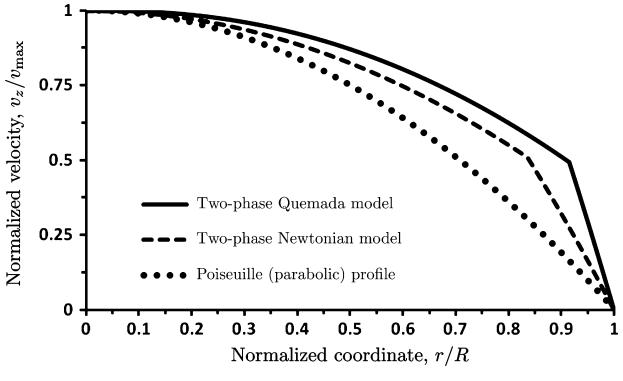

Figure 11. Normalized velocity profiles computed with the two-phase Newtonian model [21,31,33], our two-layer Quemada model, and the Poiseuille law. Each velocity $v_z(r/R)$ is normalized with its maximum (centerline) velocities v_{max}. The vessel radius is R = 20 μm and discharge hematocrit is H_d = 0.45.

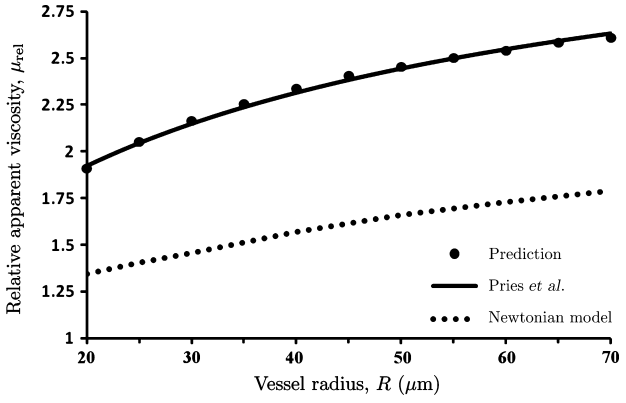

Figure 12. Dependence of relative apparent viscosity μ_{rel} on vessel radius R, computed with the two-phase Newtonian model [21,31,33], our two-layer Quemada model, and the data-fitted curve of Pries, Neuhaus, and Gaehtgens [25]. Discharge hematocrit is $H_d = 0.45$.

Newtonian model [21,31,33], our two-phase Quemada model, and the data-fitted curve (Eq. 14) of Pries, Neuhaus, and Gaehtgens [25]. The Newtonian model [21,31,33] underestimates the apparent viscosity, as compared to both our Quemada model and the experimental data in [25]. This demonstrates the importance of accounting for non-Newtonian shear-thinning behavior of the RBC-rich core.

CONSEQUENCES FOR WSS MEASUREMENTS IN BLOOD VESSELS

Measurements of WSS in arterioles are typically done (e.g., [13,28]) by employing the Poiseuille law, $Q = \pi JR^4/(8\mu)$, to express WSS $\tau_w = \tau(R)$ in terms of observable quantities such as flow rate Q, average flow velocity $v_{ave} = Q/(\pi R^2) = JR^2/(8\mu)$, or centerline velocity $v_{max} = 2v_{ave}$. This is accomplished by combining Eq. (6) with $\tau = \mu\gamma$, the Newtonian relationship between shear stress τ and shear rate $\gamma = dv_z/dr$. As for a Poiseuille flow the shear rate at the wall is given by $\gamma_w = \gamma(R) = 2v_{max}/R$, one obtains

$$\tau_{w,p} = \frac{2\mu_p v_{max}}{R}. \qquad (18)$$

Although Eq. (18) is routinely used to estimate the WSS τ_w from experiments [13,28], it is important to recognize that it is based on the assumption that blood can be treated as a homogeneous Newtonian fluid. Many theoretical and experimental studies, including our analysis in section "Simulation Results", demonstrate the importance of accounting for the non-Newtonian behavior of blood flow in microvessels. Experimental techniques, such as microparticle image velocimetry [18], enable one to obviate the need for this assumption by inferring the WSS τ_w from measurements of the entire velocity profile $v_z(r)$. However, they are expensive and operationally challenging, which hinders their *in vivo* use [13,28].

We propose an efficient alternative that utilizes standard experimental procedures to determine the discharge hematocrit H_d and a flow characteristic (Q, v_{ave}, or v_{max}), relies on the modeling algorithm in section "Algorithm for Inference of WSS from Blood Flow Measurements" to compute the wall shear rate $\gamma_w = \gamma(R)$, and makes use of the Quemada constitutive law (Eq. 1) to relate the wall shear rate γ_w to the WSS τ_w.

Algorithm for Inference of WSS from Blood Flow Measurements

Given measurements of the vessel radius R, centerline velocity v_{max}, and discharge hematocrit H_d, we employ the following algorithm to determine the WSS τ_w:

1. Set the counter to $n = 0$, the algorithm tolerance to $\varepsilon = 10^{-4}$, and the iteration factor to $k = 0.9$.
2. Compute an initial guess for the WSS $\tau_w^{(n)}$ by using the Poiseuille relation (Eq. 18).
3. Compute the corresponding values of the pressure gradient $J^{(n)} = 2\tau_w^{(n)}/R$ from Eq. (6).
4. Calculate the velocity profile $v^{(n)}(r)$ by using the algorithm in section Numerical Algorithm for Calculating Velocity Profiles with given $J^{(n)}$.
5. Compare the resulting centerline velocity ${v^{(n)}}_{max}$ with its measured value v_{max}. If

$$\left|\frac{v_{max} - v_{max}^{(n)}}{v_{max}}\right| \leq \varepsilon,$$

then go to Step 7. Otherwise, modify the value of the pressure gradient according to

$$J^{(n+1)} = \left[1 + \kappa\frac{v_{max} - v_{max}^{(n)}}{v_{max}}\right] J^{(n)}.$$

6. Set $n = n + 1$. Go to Step 4.
7. Compute the WSS $\tau_w = J^{(n)}R/2$ from Eq. (6).

For $k = 0.90$ and $\varepsilon = 0.0001$, this algorithm converged in fewer than 20 iterations in all the cases we examined.

We use the relative error $\varepsilon_{WSS} = (\tau_w - \tau_{w,P})/\tau_w$ to quantify the errors introduced by relying on the Poiseuille relation (Eq. 18) to infer the WSS ($\tau_{w,P}$), i.e., by ignoring the inhomogeneity and non-Newtonian properties of blood flow in microvessels. Figure 13 reveals that the error ε_{WSS} is significant over wide ranges of the discharge hematocrit H_d and the blood vessel radius R. This demonstrates that the Poiseuille law-based experimental inference of the WSS systematically underestimates the WSS in microcirculatory flows. The bias increases with the discharge hematocrit H_d and decreases with the vessel radius R. Both phenomena are to be expected, as they amplify the non-Newtonian behavior of the blood flow in the microcirculation (see section "Simulation Results").

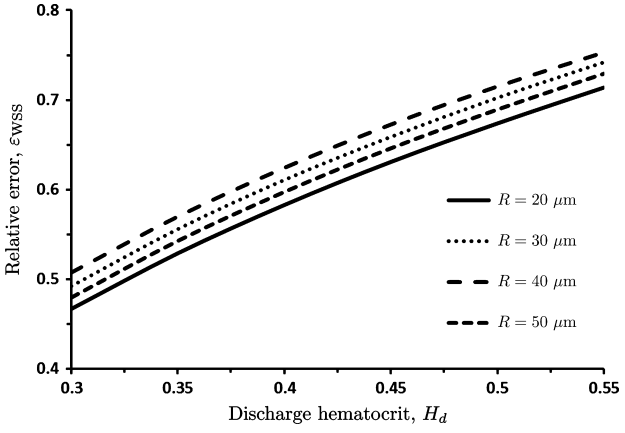

Figure 13. Relative error $\varepsilon_{WSS} = (\tau_w - \tau_{w,P})/\tau_w$ in estimation of the WSS τ_w introduced by relying on the Poiseuille relation (Eq. 18) to infer the WSS ($\tau_{w,P}$), for several values of vessel radius R.

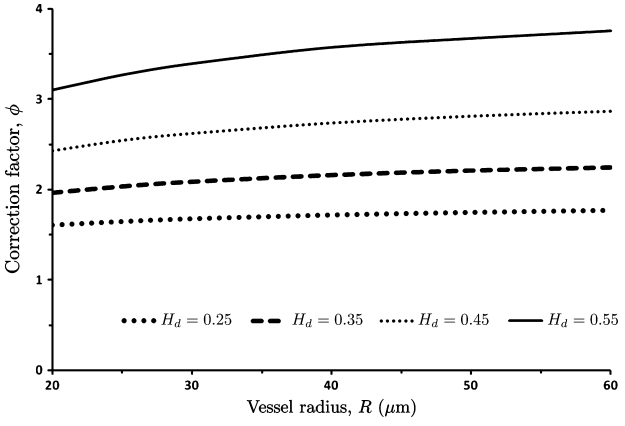

Figure 14. WSS correction factor ϕ as a function of vessel radius R, for several values of discharge hematocrit H_d.

Empirical WSS Correction Factor

The numerical algorithm described in section "Algorithm for Inference of WSS from Blood Flow Measurements" provides a rigorous means for inferring the WSS from measurements of R, H_d, and v_{max}. Here, we use it to precompute a correction factor $\phi(R, H_d)$, which would allow us to determine the WSS without resorting to numerical simulations. This correction factor enables one to determine the actual WSS τ_w from its Poiseuille law estimate $\tau_{w,P}$ given by Eq. (18) by simple multiplication, $\tau_w = \phi(R, H_d)\ \tau_{w,P}$, i.e.,

$$\tau_w = \frac{2\mu_p v_{max}}{R}\phi(R, H_d). \tag{19}$$

The correction factor $\phi(R, H_d) = \tau_w/\tau_{w,P}$ is calculated as follows. First, we employ the iterative algorithm of section "Algorithm for Inference of WSS from Blood Flow Measurements" to compute the WSS $\tau_w(R, H_d)$ for multiple values of $R \in [15, 70\ \mu m]$ and discharge hematocrit $H_d \in [0.25, 0.55]$. Then, for each of these computed values of the WSS, we obtain the correction factor as $\phi(R, H_d) = \tau_w/\tau_{w,P}$. Finally, we interpolate this $\phi = \phi(R, H_d)$ dataset with the curve (with the goodness of the fit exceeding 0.99)

$$\phi(R, H_d) = c_1 \ln R + c_0 \quad \text{where} \quad c_1 = 0.0515e^{4.732H_d},$$
$$c_0 = 0.6134H_d + 1.0548. \tag{20}$$

Figure 14 exhibits the dependence of the WSS correction factor ϕ on the vessel radius R and discharge hematocrit H_d. Equation (20) and its graphical representation in Figure 14 show that the correction factor ϕ (and, hence, the errors introduced by the reliance on the Poiseuille law) grows exponentially with the discharge hematocrit H_d. Its dependence on the vessel radius R becomes more pronounced as the discharge hematocrit H_d increases. Substituting Eq. (20) into Eq. (19) yields the modified equation for WSS estimation as a function of centerline velocity (v_{max}), vessel radius (R), plasma viscosity (μ_p), and discharge hematocrit (H_d):

$$\tau_w = \frac{2\mu_p v_{max}}{R}\left\{m_1 e^{m_2 H_d}\ln R + m_3 H_d + m_4\right\} \tag{21}$$

with $m_1 = 0.0515$, $m_2 = 4.732$, $m_3 = 0.6134$, and $m_4 = 1.0548$.

We compared the WSS values computed with Eq. (19), the iterative algorithm of section "Algorithm for Inference of WSS from Blood Flow Measurements" and the correction factor in Eq. (20) for a physiologically relevant ranges of R and H_d. This comparison reveals that the iterative algorithm and the correction factor yield the nearly identical (within 3%) estimates of WSS. Both sets of estimates are significantly higher than their counterparts predicted with the Poiseuille relation (Eq. 18).

The results presented in this study are obtained for parameter values typical of human blood. Therefore, they are applicable both for *in vitro* experiments in glass tubes [18] and tissue cultures [20], and for *in vivo* observations such as retinal [30] or MRI [6] studies. For experiments that involve blood from other species, the approach used in this study may be replicated with suitable rheological data for the type of blood under consideration as an input. This would require the measurements of the dependence of the CFL thickness δ on H_d and R, and blood rheology data (which is readily available in the literature for a number of species).

DISCUSSION

We presented a two-layer blood flow model that accounts for a non-Newtonian RBC core layer and a Newtonian CFL near the vessel wall. The rheology of the RBC core was modeled using the Quemada model [19,22,26] which accurately

describes the shear-thinning properties of blood over a large range of shear rates and hematocrits. Each fluid layer was assumed homogeneous and immiscible, with the resulting flow assumed to be laminar and axisymmetric.

To calculate velocity profiles using this model, we assumed a general functional form of the CFL thickness δ as a function of discharge hematocrit H_d. We then used Eqs. (7–11) to calculate flow velocities, flow rates, and relative apparent viscosity μ_{rel}. We calibrated our expression for δ, given by Eq. (11), so that our predictions for apparent viscosity at different hematocrits and radii were in agreement with the work of Pries, Neuhaus, and Gaehtgens [25]. Figure 5 shows that our model was able to match the predictions of Pries, Neuhaus, and Gaehtgens [25] providing validation to the assumption that δ is an almost linear function of discharge hematocrit and is independent of tube radius.

We were further able to validate our model by comparing (i) the predicted velocity profiles with experimental data [18], (ii) the predicted hematocrit ratio H_t/H_d vs values reported in the literature (both experimental data and numerical models), and (iii) δ/R values with those estimated in experimental studies [24,27,35].

Agreement between our calculated and measured velocity profiles [18] is shown in Figure 7. The calculated values of velocity, shape of velocity profile, and CFL thickness are in reasonable agreement with experiments (see section "Model Validation"). Furthermore, our predictions for H_t/H_d fall within the broad range of values suggested in the literature (Figure 8). The scatter in the range of values reported is unfortunately rather large, with very few experiments carried out in recent years with modern experimental techniques. New experiments to measure tube vs discharge hematocrit would help better calibrate flow models of blood flow in microvessels.

Our predictions of CFL thickness δ also seem to be in reasonable agreement with experiments [14,24,27,35]. Our estimates of δ are closer to the experimentally observed values than those reported in other theoretical studies [9,31,33]. The range of δ predicted for physiological levels of hematocrit (in the vicinity of 0.45) falls between 1.5 and 3 μm in most experimental studies. Our predictions of δ in the range 2.5–1.8 μm over a range of hematocrits from 0.35 to 0.55 are within this range of experimentally measured values. Figure 6 shows that our estimates of δ/R vs R for $H_d = 0.45$ are in general agreement with the experimental observations [24,27,35].

We demonstrated the resulting dependence of core hematocrit H_c on discharge hematocrit H_d in small- to intermediate-sized arterioles, as shown in Figure 10. As the vessel size increases, the importance of the Fahraeus effect [8] reduces and core and systemic hematocrit become essentially indistinguishable, due to the fact that the width of the cell-depleted layer becomes negligible compared to vessel radius. Hence, we expect core hematocrit to be almost the same as discharge hematocrit in large blood vessels (where the core is essentially the entirety of the vessel cross section), but in smaller blood vessels the core hematocrit should be significantly elevated over systemic (or discharge) hematocrit.

We examined whether our model makes predictions that are different from the Newtonian model of blood flow used previously in [21,31,33]. Figure 11 provides a comparison of our predictions of the velocity profiles with those computed with the two-layer Newtonian model, for the vessel radius $R = 20$ μm and the pressure gradient $J = 40{,}000$ dyn/cm^3. Our two-layer non-Newtonian model predicts significantly smaller axial velocities and blunter velocity profiles than the two-layer Newtonian model does. Sharply blunted velocity profiles are commonly reported in the experimental literature [1,3,10,15,18,36].

We also analyzed the dependence of the relative apparent viscosity on the vessel radius (see Figure 12, for $H_d = 0.45$). The Newtonian model significantly underestimates the relative apparent viscosities both predicted with our model and observed experimentally (see the data in [25]). As with a single optimized set of parameters our model is able to simultaneously predict realistic values of apparent viscosity, CFL thickness, tube hematocrit, and velocity profiles that are in broad agreement with the experimental literature, we submit that our model is a significant improvement over prior Newtonian flow models.

The blunting of velocity profiles discussed in this study has a number of consequences. Typical *in vivo* measurements of WSS in the microcirculation are based on the Poiseuille relation (Eq. 18), which assumes the Newtonian behavior and results in parabolic velocity profiles [13,28]. The errors introduced by this assumption lead to a significant underestimation of WSS. Specifically, as shown in Figure 13, the relative error in using the Poiseuille relation (Eq. 18) increases with increasing values of discharge hematocrit H_d (as increasing H_d greatly amplifies the non-Newtonian nature of the flow); for $H_d = 0.45$, the use of the Poiseuille relation underestimates WSS by approximately 60–65%, across a broad range of vessel radii. Even at a smaller, but physiologically relevant $H_d = 0.30$, WSS was found to be underestimated by over 45% when applying the Poiseuille relation.

We proposed two methods to eliminate these errors: An iterative numerical algorithm which leverages our flow model, and the use of a simple correction factor that can be incorporated into the Poiseuille law. Given a rheological model of the RBC-rich core, both approaches allow the inference of WSS from measurements of vessel radius, centerline velocity, and discharge hematocrit. As the WSS values calculated with these two methods differ by approximately 3%, one can rely on the correction factor without sacrificing the measurement accuracy. This correction factor

varies with the discharge hematocrit H_d and vessel radius R, as shown in Figure 14. The proposed approach is also useful in models where WSS is an input for calculations of quantities, such as shear-induced NO production [32,33].

This analysis and the proposed correction factors should aid in evaluating the changes in shears stress induced by the changes in the composition of blood due to the application of plasma expanders that affect the blood's shear-thinning properties [32]. The effects of this type of transfusional intervention appear to be significantly dependent on the rheological changes induced in diluted blood and are becoming the focus of research and development in designing new transfusion strategies [4].

PERSPECTIVE

The mathematical model of blood flow in microvessels presented in this study allows for prediction of velocity profiles and CFL thicknesses that were validated against previously published experimental data. The blunted velocity profiles occur due to both the non-Newtonian and nonhomogeneous nature of blood flow in microvessels; both factors are accounted for in our model. Typically, the estimation of WSS in experimental studies is achieved through measurement of vessel centerline velocity and radius, followed by the application of the Hagen–Poiseuille law. Due to the non-Newtonian and nonhomogeneous nature of blood, using the Hagen–Poiseuille law introduces significant errors in WSS estimation. Using the flow model presented in this study, a correction factor to the Hagen–Poiseuille law was derived to eliminate these errors; allowing for accurate estimation of WSS in experiments.

ACKNOWLEDGMENTS

This study was supported in part by USPHS NIH 5P01 HL110900, J.M. Friedman PI., and United States Army Medical Research Acquisition Activity Contract W81XWH1 120012, A.G. Tsai PI.

REFERENCES

1. Alonso C, Pries AR, Kiesslich O, Lerche D, Gaehtgens P. Transient rheological behavior of blood in low-shear tube flow: velocity profiles and effective viscosity. *Am J Physiol* 268: H25–H32, 1995.
2. Baskurt OK, Hardeman MR, Rampling MW, Meiselman HJ. *Handbook of Hemorheology and Hemodynamics, 69 of Biomedical and Health Research*. Amsterdam, Netherlands: IOS Press, 2005.
3. Bishop JJ, Nance PR, Popel AS, Intaglietta M, Johnson PC. Effect of erythrocyte aggregation on velocity profiles in venules. *Am J Physiol Heart Circ Physiol* 280: H222–H236, 2001.
4. Cabrales P, Intaglietta M. Blood substitutes: evolution from noncarrying to oxygen and gas carrying fluids. *ASAIO J* 59: 337–354, 2013.
5. Cabrales P, Tsai AG, Intaglietta M. Alginate plasma expander maintains perfusion and plasma viscosity during extreme hemodilution. *Am J Physiol Heart Circ Physiol* 288: H1708–H1716, 2005.
6. Cheng CP, Herfkens RJ, Taylor CA. Abdominal aortic hemodynamic conditions in healthy subjects aged 50-70 at rest and during lower limb exercise: in vivo quantification using MRI. *Atherosclerosis* 168: 323–331, 2003.
7. Chien S, Usami S, Taylor HM, Lundberg JL, Gregersen MI. Effects of hematocrit and plasma proteins on human blood rheology at low shear rates. *J Appl Physiol* 21: 81–87, 1966.
8. Fahraeus R. The suspension stability of blood. *Physiol Rev* 9: 562–568, 1929.
9. Fedosov DA, Caswell B, Popel AS, Karniadakis GE. Blood flow and cell-free layer in microvessels. *Microcirculation* 17: 615–628, 2010.
10. Gaehtgens P, Meiselman HJ, Wayland H. Velocity profiles of human blood at normal and reduced hematocrit in glass tubes up to 130 mm diameter. *Microvasc Res* 2: 13–23, 1970.
11. Hochmuth RM, Davis DO. Changes in hematocrit for blood flow in narrow tubes. *Bibl Anat* 10: 59–65, 1969.
12. Jendrucko RJ, Lee JS. The measurement of hematocrit of blood flowing in glass capillaries by microphotometry. *Microvasc Res* 6: 316–331, 1973.
13. Katritsis D, Kaiktsis L, Chaniotis A, Pantos J, Efstathopoulos EP, Marmarelis V. Wall shear stress: theoretical considerations and methods of measurement. *Prog Cardiovasc Dis* 49: 307–329, 2007.
14. Kim S, Kong RL, Popel AS, Intaglietta M, Johnson PC. Temporal and spatial variations of cell-free layer width in arterioles. *Am J Physiol Heart Circ Physiol* 293: H1526–H1535, 2007.
15. Koutsiaris AG. A velocity profile equation for blood flow in small arterioles and venules of small mammals in vivo and an evaluation based on literature data. *Clin Hemorheol Micro* 43: 321–334, 2009.
16. Ku DN. Blood flow in arteries. *Ann Rev Fluid Mech* 29: 399–434, 1997.
17. Lipowsky HH, Kovalcheck S, Zweifach BW. The distribution of blood rheological parameters in the microvasculature of cat mesentery. *Circ Res* 43: 738–749, 1978.
18. Long DS, Smith ML, Pries AR, Ley K, Damiano ER. Microviscometry reveals reduced blood viscosity and altered shear rate and shear stress profiles in microvessels after hemodilution. *Proc Natl Acad Sci USA* 101: 10060–10065, 2004.
19. Marcinkowska-Gapinska A, Gapinski J, Elikowski W, Jaroszyk F, Kubisz L. Comparison of three rheological models of shear flow behavior studied on blood samples from post-infarction patients. *Med Biol Eng Comput* 45: 837–844, 2007.
20. Mashour GA, Boock RJ. Effects of shear stress on nitric oxide levels of human cerebral endothelial cells cultured in an artificial capillary system. *Brain Res* 842: 233–238, 1999.
21. Nair PK, Hellums JD, Olson JS. Prediction of oxygen transport rates in blood flowing in large capillaries. *Microvasc Res* 38: 269–285, 1989.
22. Oliver JD. The viscosity of human blood at high hematocrits. Master's thesis, MIT, 1986.
23. Popel AS, Johnson PC. Microcirculation and hemorheology. *Ann Rev Fluid Mech* 37: 43–69, 2005.
24. Pries AR, Kanzow G, Gaehtgens P. Microphotometric determination of hematocrit in small vessels. *Am J Physiol Heart Circ Physiol* 245: H167–H177, 1983.
25. Pries AR, Neuhaus D, Gaehtgens P. Blood viscosity in tube flow: dependence on diameter and hematocrit. *Am J Physiol Heart Circ Physiol* 263: H1770–H1778, 1992.

26. Quemada D. Rheology of concentrated dispersed systems: III. General features of the proposed non- Newtonian model: comparison with experimental data. *Rheol Acta* 17: 643–653, 1978.
27. Reinke W, Gaehtgens P, Johnson PC. Blood viscosity in small tubes: effect of shear rate, aggregation, and sedimentation. *Am J Physiol Heart Circ Physiol* 253: H540–H547, 1987.
28. Reneman RS, Arts T, Hoeks AP. Wall shear stress–an important determinant of endothelial cell function and structure–in the arterial system in vivo. Discrepancies with theory. *J Vasc Res* 43: 251–269, 2006.
29. Richter V, Savery MD, Gassmann M, Baum O, Damiano ER, Pries AR. Excessive erythrocytosis compromises the blood-endothelium interface in erythropoietin-overexpressing mice. *J Physiol* 589: 5181–5192, 2011.
30. Riva CE, Grunwald JE, Sinclair SH. Laser doppler velocimetry study of the effect of pure oxygen breathing on retinal blood flow. *Invest Ophthalmol Vis Sci* 24: 47–51, 1983.
31. Sharan M, Popel AS. A two-phase model for flow of blood in narrow tubes with increased effective viscosity near the wall. *Biorheology* 38: 415–428, 2001.
32. Sriram K, Salazar V'azquez BY, Tsai AG, Cabrales P, Intaglietta M, Tartakovsky DM. Autoregulation and mechanotransduction control the arteriolar response to small changes in hematocrit. *Am J Physiol Heart Circ Physiol*, 303: H1096–H1106, 2012.
33. Sriram K, Salazar V'azquez BY, Yalcin O, Johnson PC, Intaglietta M, Tartakovsky DM. The effect of small changes in hematocrit on nitric oxide transport in arterioles. *Antioxid Redox Signal*, 14: 175–185, 2011.
34. Sriram K, Tsai AG, Cabrales P, Meng F, Acharya SA, Tartakovsky DM, Intaglietta M. PEG albumin supra plasma expansion is due to increased vessel wall shear stress induced by blood viscosity shear thinning. *Am J Physiol Heart Circ Physiol* 302: H2489–H2497, 2012.
35. Suzuki Y, Tateishi N, Soutani M, Maeda N. Flow behavior of erythrocytes in microvessels and glass capillaries: effects of erythrocyte deformation and erythrocyte aggregation. *Int J Microcirc Clin Exp* 16: 187–194, 1996.
36. Tangelder GJ, Slaaf DW, Reneman RS. Velocity profiles of blood platelets and red blood cells flowing in arterioles of the rabbit mesentery. *Circ Res* 59: 505–514, 1986.

APPENDIX

Two-phase Newtonian model for flow velocity

According to the two-phase Newtonian model of blood flow [31,33], the velocity distribution in a microvessel of radius R is given by

$$v_z(\xi) = \frac{JR^2}{4\mu_p}\begin{cases} 1-\lambda^2+\frac{\mu_p}{\mu_c}(\lambda^2-\xi^2) & \text{for } 0\le\xi\le\lambda \\ 1-\xi^2 & \text{for } \lambda<\xi\le 1 \end{cases} \tag{22}$$

where μ_c is the viscosity of the RBC-rich core, $\xi = r/R$ and $\lambda = 1-\delta/R$. When expressed in μm, the CFL width δ is given by [33]

$$\delta = -7.55H_d + 6.91. \tag{23}$$

For human blood, μ_c is calculated as [31]

$$\frac{\mu_c(H_c)}{\mu_p} = 1 + 2.2\frac{(1-H_c)^{-0.8}-1}{(1-0.45)^{-0.8}-1}. \tag{24}$$

Finally, the core hematocrit H_c is related to the discharge hematocrit H_d by [31,33]

$$H_c\int_0^{1-\lambda} v_z(\xi)\xi d\xi = H_d\int_0^1 v_z(\xi)\xi d\xi. \tag{25}$$

The resulting set of equations is solved by following the procedure described in [33].